Materials Science & Engineering A 897 (2024) 146316

Contents lists available at ScienceDirect

Materials Science & Engineering A

journal homepage: www.elsevier.com/locate/msea

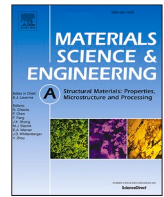

Microscopic fracture toughness of notched porous sintered Cu micro-cantilevers for power electronics packaging

Dong Hu [a], Leiming Du [a], Markus Alfreider [b,*], Jiajie Fan [a,c], Daniel Kiener [b], Guoqi Zhang [a,**]

[a] Department of Microelectronics, Delft University of Technology, 2628 CD, Delft, the Netherlands
[b] Department of Materials Science, Montanuniversität Leoben, Leoben, Austria
[c] Shanghai Engineering Technology Research Center for SiC Power Device, Academy for Engineering & Technology, Fudan University, Shanghai, 200433, China

ARTICLE INFO

Keywords:
Cu nanoparticles sintering
Continuous stiffness testing
Elastic-plastic fracture mechanics
Microscopic fracture toughness

ABSTRACT

To fulfill the high-temperature application requirement of high-power electronics packaging, Cu nanoparticle sintering technology, with benefits in low-temperature processing and high-melting point, has attracted considerable attention as a promising candidate for the die-attach interconnect. Comprehensive mechanical characterization of the sintered layer at a microscale is necessary to deepen the understanding of the fracture behavior and improve the reliable design of materials. In this study, microscale cantilevers with different notch depths were fabricated in a 20 MPa sintered interconnect layer. Continuous dynamical fracture testing of the microcantilevers was conducted *in situ* in a scanning electron microscope to detail the failure characteristic of the porous sintered structure. The microscopic fracture toughness of different notched specimens was obtained from the *J*-integral in the frame of elastic-plastic fracture mechanics. Specimens with deeper notches presented higher resistance to crack extension, while geometry factors of notch-to-width ratio between 0.20 and 0.37 exhibited a relatively stable microscopic fracture toughness ranging from 3.2 ± 0.3 to 3.6 ± 0.1 MPa m$^{1/2}$.

1. Introduction

As one critical strategic direction in the More than Moore (MtM) concept, power electronics is undergoing rapid development contributed by industrial electrification [1]. In the U.S. Department of Energy's roadmap for 2025, 33 kW/L power density and 300,000 mile/15-year lifetime are targeted in a 100 kW electric traction power converter [2]. Due to the physical limit of silicon (Si)-based devices, wide-bandgap semiconductors (WBG), represented by silicon carbide (SiC) and gallium nitride (GaN), have been proposed as the promising alternative according to its compelling advantages, such as high breakdown voltage, high operating temperature, high switching frequency and low loss [3,4]. Considering ~200 °C–250 °C operating junction temperature in the WBG devices, the high-temperature degradation of a necessary die-attach layer, which is the closest layer to get the heat away from a die, becomes a critical challenge regarding reliability performance [5,6].

In the past decade, Sn-based solders and metallic nanoparticles have been the most promising Pb-free die-attach materials, according to RoHS (Restriction of Hazardous Substances) [5,7]. In high-temperature packaging, high operating temperature results in a costy high-temperature soldering process. In an extreme case of an operating temperature exceeding 500 °C, none of the known solders can work [8]. However, nanoparticle sintering technology, as established for Ag and Cu, takes advantage of low-processing temperatures and robust high-temperature stability as the sintered structure shares close melting point with its bulk status. Compared to the soldering technology, the nanoparticle sintering technology gets no involvement of unwanted brittle intermetallic compounds (IMC) while also more excellent thermal and electrical conductivity. Several reports have reported different Ag sintering technologies for various concepts of power modules [9–11]. However, sintered Ag joints are prone to mass migration, risking reliability performance in the long-term operation [12]. As an alternative, sintered nanoporous Cu also presents excellent electrical and thermal performance and is even more cost-effective than Ag. Recently, beneficial Cu nanomaterial-based packaging solutions have been reported for high power density and junction temperature [13,14].

Besides the intensive development of the materials composition and process optimization, understanding the mechanical properties of the sintered layer is also essential for the design for reliability (DfR), where an

* Corresponding author.
** Corresponding author.
E-mail addresses: Markus.Alfreider@unileoben.ac.at (M. Alfreider), G.Q.Zhang@tudelft.nl (G. Zhang).

https://doi.org/10.1016/j.msea.2024.146316
Received 18 December 2023; Received in revised form 28 February 2024; Accepted 29 February 2024
Available online 7 March 2024
0921-5093/© 2024 The Authors. Published by Elsevier B.V. This is an open access article under the CC BY license (http://creativecommons.org/licenses/by/4.0/).

accurate material model is needed as a key input to predict the failure of the entire system. The porous die-attach layer manufactured by sintering technology presents mechanical properties and deformation behavior different from the bulk metal, depending on the post-sintering residual porosity. Typically, the mechanical performance of the sintered joint is characterized at the macroscopic scale by employing shearing and bending tests [15–17]. However, these are not rigorous measurement methods to obtain local fracture toughness and improve understanding of the fracture behavior in the sintered layer. Fracture toughness is a crucial parameter for assessing the failure behavior by describing the ability of materials containing a pre-existing notch to resist crack propagation. A computational modeling approach has been suggested to calculate the stress intensity in a sandwich-lick sintered joint through finite element analysis (FEA) at points along the crack growth path [18]. However, an accurate set of material properties was required to input the model. From an experimental perspective, Wang et al. studied the interfacial fracture toughness of sintered hybrid silver interconnect using modified compact tension experiments, revealing that the pore size and porosity significantly influenced the fracture resistance [19]. Zhao et al. employed an end notch flexure (ENF) test to determine sintered Ag's mode II shearing fracture toughness considering various sintering temperatures and holding time [20]. Based on the developed ENF method, Dai et al. further parameterized mode II cohesive zone models in the sintered Ag joint with additive carbon nanotube [21].

However, it has been extensively demonstrated that the mechanical properties at a macro-scale can differ dramatically from the microscopic properties due to the existence of a size effect [22]. Consequently, macroscopic data is insufficient for a safe design of microelectronic structures. Considering the practical dimension of a die-attach layer of ~10 μm, plenty of features remain to be explored at the micro-scale, and the local fracture toughness (K_{IC}) of nanoporous Cu as a die-attach layer is one of them.

Recently, focussed ion beam (FIB) fabricated micro-cantilever (MC) bending tests have been reported as a helpful tool to evaluate the mode I fracture toughness at the microscale [23]. Furthermore, Wurster et al. improved the understanding of fracture experiments using notched MC and proposed a general measurement methodology at the microscale using the *J*-integral and the related crack tip opening displacement (CTOD) [24]. At present, MC bending fracture experiments have been utilized for die-attach interconnects, including AgSn solder [25], CuSn solder [26], sintered Ag microparticles [27], and sintered Cu nanoparticles [28]. Regarding the latter two sintering technologies, a ductile fracture was revealed, accompanied by local necking at the crack tip. However, when the component size approaches to the range of actual bondline thickness of a few tens micrometers, the effect of the test condition, *e.g.*, notch depth, on the potentially component size-dependent fracture toughness is underexplored, while a reliable estimation of mechanical failure at the microscale is essential.

In the present work, the fracture toughness of pressure-sintered Cu joints with a continuous porous network was investigated using MC specimens at the microscale. These MCs were micro-fabricated by an FIB perpendicular to the direction of the applied sintering pressure with different notch depths to study the effect of the notch depth on the fracture toughness and crack propagation behavior at the microscale. Therefore, the *J*-integral versus crack extension (J-Δa) curves were translated from the load-displacement curves. Afterward, the microscopic conditional fracture toughness was extracted from elastic-plastic *J*-integral evaluation and then compared to the relevant works. This work provides insights into package-level modeling by exploring the fracture behavior and fracture toughness of the sintered Cu joint.

2. Experimental methodology

2.1. Material preparation

This study examines a self-made nano Cu paste with the process flow reported in Ref. [29]. The paste contained quasi-spherical Cu nanoparticles with an average diameter of 100 ± 36 nm. The fabrication process of the sintered specimen is illustrated in Fig. 1. At first, the self-made Cu paste was dispensed into a steel mold with a 5 mm × 5 mm opening using a metal squeegee. Afterward, the paste and mold were dried in an oven at 120 °C for 15 min. This step helped evaporate the organic solvent in the paste composition, reducing the risk of air bubble generation during the sintering process. To mimic the actual operation conditions, the dried paste was sintered at 250 °C for 10 min with a rapid heating rate of 50 °C/min. Constant uniaxial pressure of 20 MPa was maintained to promote the sintering within a constant N_2 atmosphere to prevent oxidation. The sintered cubic specimen had dimensions of 5 mm × 5 mm and approximately 1 mm thickness.

2.2. Micro-cantilever bending tests

As shown in Fig. 2, the micro-cantilevers were microfabricated on the sintered specimen using a dual-beam scanning electron microscope (SEM)/FIB microscope (FEI Helios G4Cx) with an accelerating voltage of 30 kV. The position of the MCs was chosen at the sintered specimen edge, which simplified the pre- and post-test microstructure characterization. At first, a cleaning cut was applied to remove defects on the edge. Afterward, coarse milling with an ion current ranging from 21 nA down to 2.5 nA was applied to shape the cantilevers quickly. However, due to the local heat brought by the large ion current, the near-surface was fused. In order to remove the fused surface, the cantilevers subsequently experienced fine milling with a small ion current at pAs. During the coarse milling and fine milling, the specimen has to be taken out and placed again with 90° rotation. Thus, all faces of the cantilever were well polished by FIB. The notches were cut at last with a 24 pA ion current, reducing the width of the notch. The dimensions of the MC are outlined in Table 1. It should be noticed that a certain amount of reliable error (~0.02 μm) is included in the dimension measurement when identifying the edge of the cantilever. The geometric dimensions of the MC are indicated in Fig. 2, where a, L, L_{eff}, W, and B denoted notch depth, cantilever length to tip, effective crack-to-tip length, cantilever width, and cantilever height, respectively. In this study, while one specimen remained unnotched, for the others, the notch was cut on the top surface of the cantilever to result in four different a/W ratios: 0, 0.2, 0.37, and 0.5 of the cantilever height, respectively. Additionally, a high aspect ratio of 3.5 was designed for cantilever fabrication. Therefore, a linear elastic bending theory can be adopted. Three MCs were prepared per condition.

Subsequently, the fabricated MCs were loaded in a dual beam FIB/SEM workstation (Leo 1540XB, Carl Zeiss AG, Oberkochen, Germany) using a Hysitron picoindenter PI85 (Bruker Corporation, Billerica, USA) with a nanoDMA III upgrade for continuous stiffness measurement. All specimens were manually aligned and tested using a wedge-shaped conductive diamond tip indenter (Synton-MDP, Nidau, Switzerland). A constant loading rate of 10 μN/s and a constant superimposed sinusoidal 80 Hz signal with amplitude of 5 μN for continuous stiffness measurements were chosen for all specimens [30]. The force and indenter displacement, as well as continuous *in situ* SEM micrographs, were recorded for data post-processing during the bending test.

2.3. Fracture toughness evaluation

The stress intensity factor is a function of applied stress, component geometry, and crack length. Failure or facture is inevitable when the stress intensity factor exceeds the fracture toughness regarding the Griffith and Irwin fracture criterion [31]. In terms of evaluating the *J*-integral in the framework of elastic-plastic fracture mechanics, the following iterative method described in ASTM E1820 was applied [32]. Despite ATSM 1820 not being valid in its full extent for microscopic specimens, it is generally accepted in the community as the closest analogy to valid macroscopic testing, where non-linear elastic

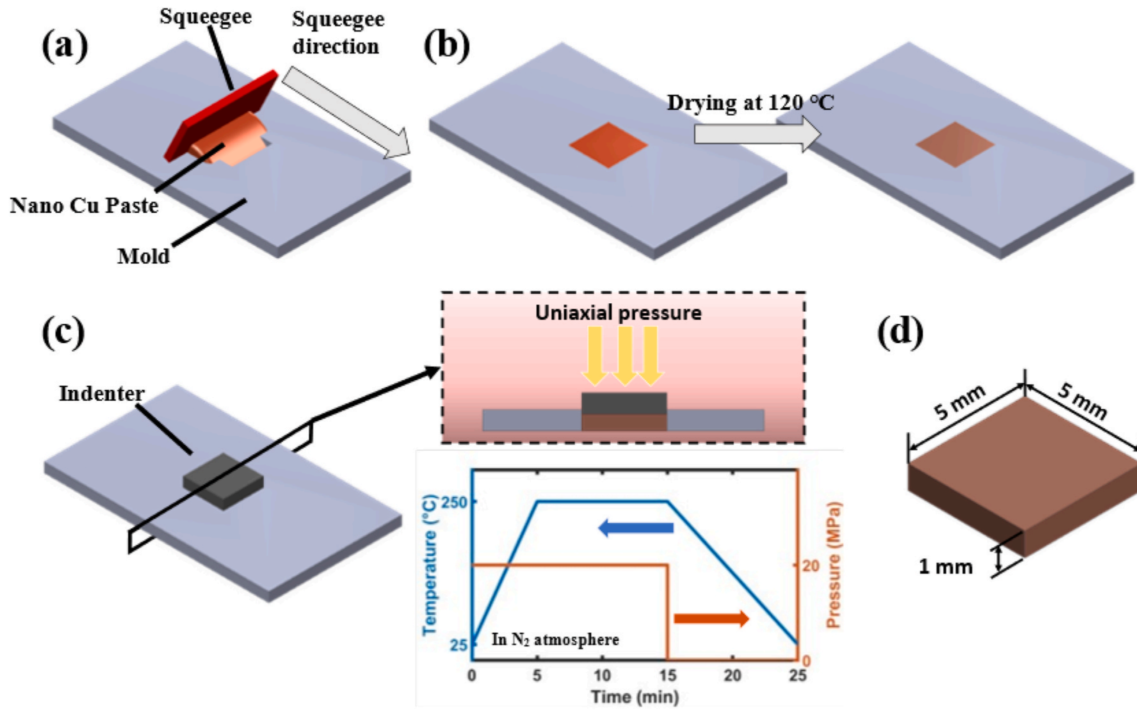

Fig. 1. Pressure-assisted sintering process for specimen fabrication: (a) paste dispersion, (b) paste drying, (c) pressure-assisted sintering, and (d) specimen dimension.

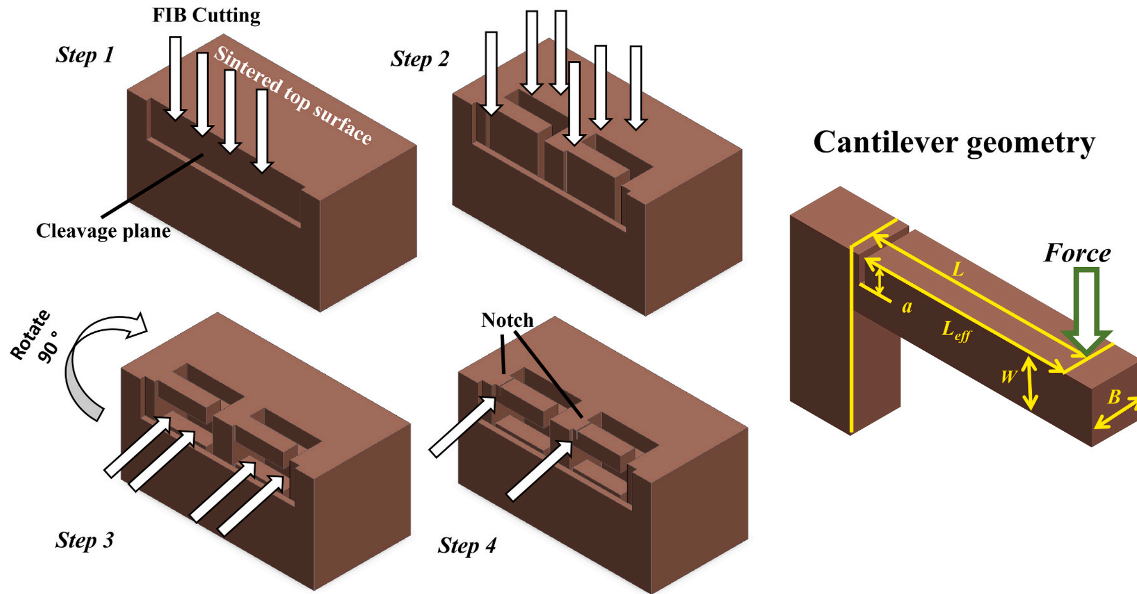

Fig. 2. FIB cutting process and dimensional notation. Notch depth a, cantilever length to tip L, effective crack-to-tip length L_{eff}, cantilever width W, and cantilever height B, as given in Table 1, are indicated. The position of the application of force is pointed.

phenomena are present.

$$J(a) = J^{el}(a) + J^{pl}(a) \tag{1}$$

$$J_n^{el} = \frac{K_{q,n}^2(1-\nu^2)}{E} \tag{2}$$

$$J_n^{pl} = \left\{ J_{n-1}^{pl} + \frac{\eta_n}{W-a_n} \frac{A_n^{pl} - A_{n-1}^{pl}}{B} \right\} \left\{ 1 - \gamma_n \frac{a_n - a_{n-1}}{W-a_n} \right\} \tag{3}$$

where $J^{el}(a)$ and $J^{pl}(a)$ are the elastic and plastic J-integral values at specific crack lengths a, and n denotes the number of iteration steps. The respective crack lengths were calculated from the dynamic compliance signal based on an analytic solution outlined in Refs. [33,34].

$$\int_0^a \frac{a}{W} f\left(\frac{a}{W}\right)^2 da = \frac{(k_0/k - 1)L}{18\pi(1-\nu^2)r^2} \tag{4}$$

where a is the crack length, W and L are geometric parameters, k and k_0 are the stiffness of the cracked and unnotched beam respectively, ν is Poisson's ratio and $f(a/W)$ is a geometry factor that for the given cantilever geometry [35], as:

Table 1
The dimensions of MC beams were measured from SEM.

Specimen	a/W	a (μm)	L (μm)	L_{eff} (μm)	W (μm)	B (μm)
aW0-01	/	/	13.39	/	3.85	4.13
aW0-02	/	/	13.95	/	4.03	4.22
aW0-03	/	/	13.66	/	3.98	4.10
aW20-01	0.21	0.87	13.00	12.01	4.17	4.31
aW20-02	0.20	0.78	14.13	13.03	3.93	4.31
aW20-03	0.19	0.77	14.13	13.07	4.06	4.39
aW37-01	0.37	1.39	14.08	13.1	3.77	4.18
aW37-02	0.36	1.4	13.97	13.07	3.86	4.22
aW37-03	0.37	1.43	14.16	12.97	3.91	4.5
aW50-01	0.50	1.75	13.4	12.2	3.5	3.94
aW50-02	0.52	1.82	12.53	11.47	3.48	4.96
aW50-03	0.50	1.86	13.49	12.41	3.7	4.33

$$f\left(\frac{a}{W}\right)=\sqrt{\frac{2w}{\pi a}\tan\left(\frac{\pi a}{2w}\right)}\frac{0.923+0.199\left(1-\sin\left(\frac{\pi a}{2w}\right)\right)^4}{\cos\left(\frac{\pi a}{2w}\right)} \tag{5}$$

Subsequently, the stress intensity factor K_q was calculated using [35].

$$K_{q,n}=\frac{6F_nL_{eff}}{BW^2}\sqrt{\pi a_n}f\left(\frac{a_n}{W}\right) \tag{6}$$

Here, B, W, a, and L_{eff} are geometric dimensions defined in Fig. 2 and F is the load.

The plastic part of the J-integral was calculated using recommended geometry-independent prefactors $\eta = 1.9$ and $\gamma = 0.9$ in ASTM 1820 [32]. It should be noticed that the value of η and γ can be slightly affected by the a/W ratio, while in this study, a constant value was assumed for simplification [36]. A^{pl} is the plastic work computed from the recorded load-displacement curves as Eq. (7) [30]

$$A_n^{pl}=\int_0^{u_n}Fdu-\frac{F_n^2}{2k_n} \tag{7}$$

where u_n, F_n, and k_n are the respective displacements, load, and stiffness. The dynamic stiffness k was calculated as the inverse of the dynamic compliance $k = c^{-1}$.

3. Results

3.1. Microstructure and fracture charactersistics of sintered Cu micro-cantilevers

Fig. 3(a) depicts the microstructure after sintering. A typical nano-porous (NP) sintered structure is present, with developed inter-particle connections and occasional twin boundaries crossing entire grains. The line intercept technique was employed to evaluate the average grain size, calculated as 0.24 μm ± 0.04 μm by randomly drawing lines and not accounting the pores. In addition, to estimate the porosity of the sintered structure while eliminating the error within single 2D images, a 3D sampling was carried out by slicing the specimens with 50 nm spacing, as depicted in Fig. 3(b). From this sequential data, a Gaussian filter was applied to improve the image contrast. The phase segmentation of the sintered Cu and the pores was implemented based on a thresholding method, as shown in Fig. 3(c). Consequently, a 3D model was reconstructed and rendered in the commercial software AVIZO [37]. The absolute porosity was then defined by the ratio of the total pore volume to that of the volume of interest (VOI). The average absolute porosity of the sintered structure is 8.25 ± 0.69 %.

Fig. 4(a)-(d) depicts the MC beams with different a/W ratios before the bending test. It can be seen that the side view of the MC beams is rectangular, and the notches are parallel to the loading direction. The crack propagation of MC beams with a/W of 0.2 before and after the bending test is presented in Fig. 4(e)–(g) as an example. Before the bending (Fig. 4(e)), the crack is parallel to the direction of the

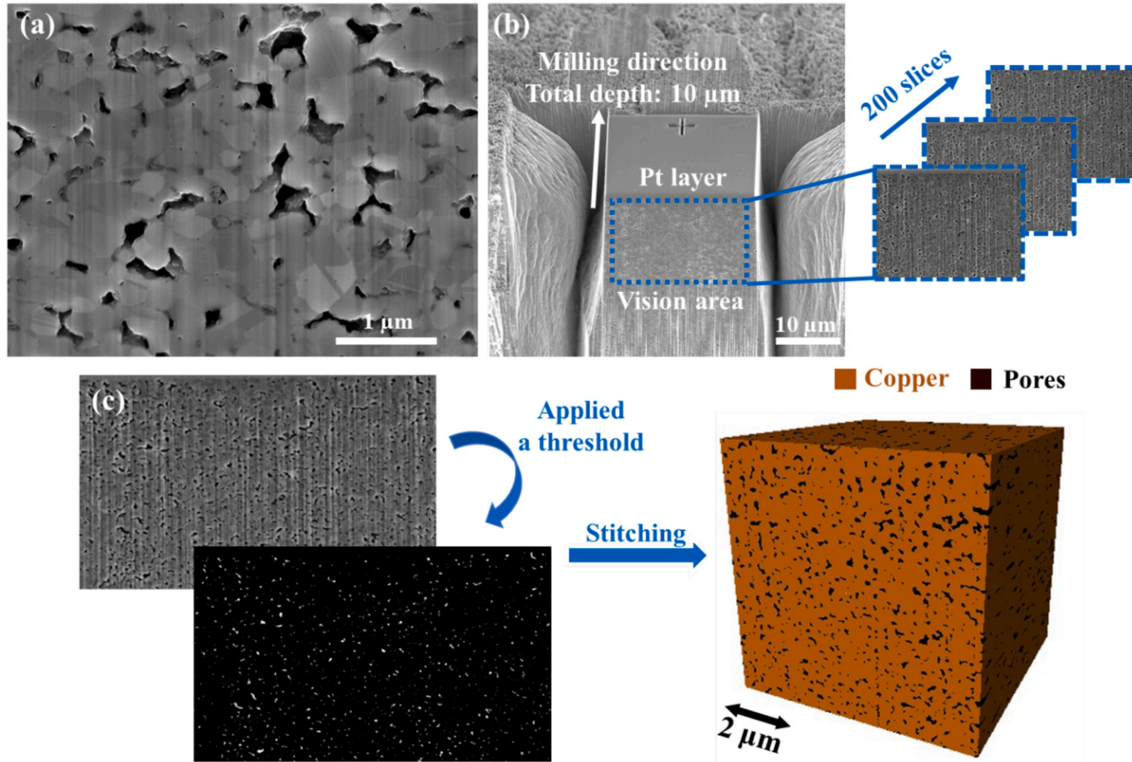

Fig. 3. (a) Micrograph of the sintered structure, depicting pores and individual grains. (b) FIB slicing for porosity calculation. (c) Rendered binary 3D VOI with copper and pore phase by means of a thresholding method.

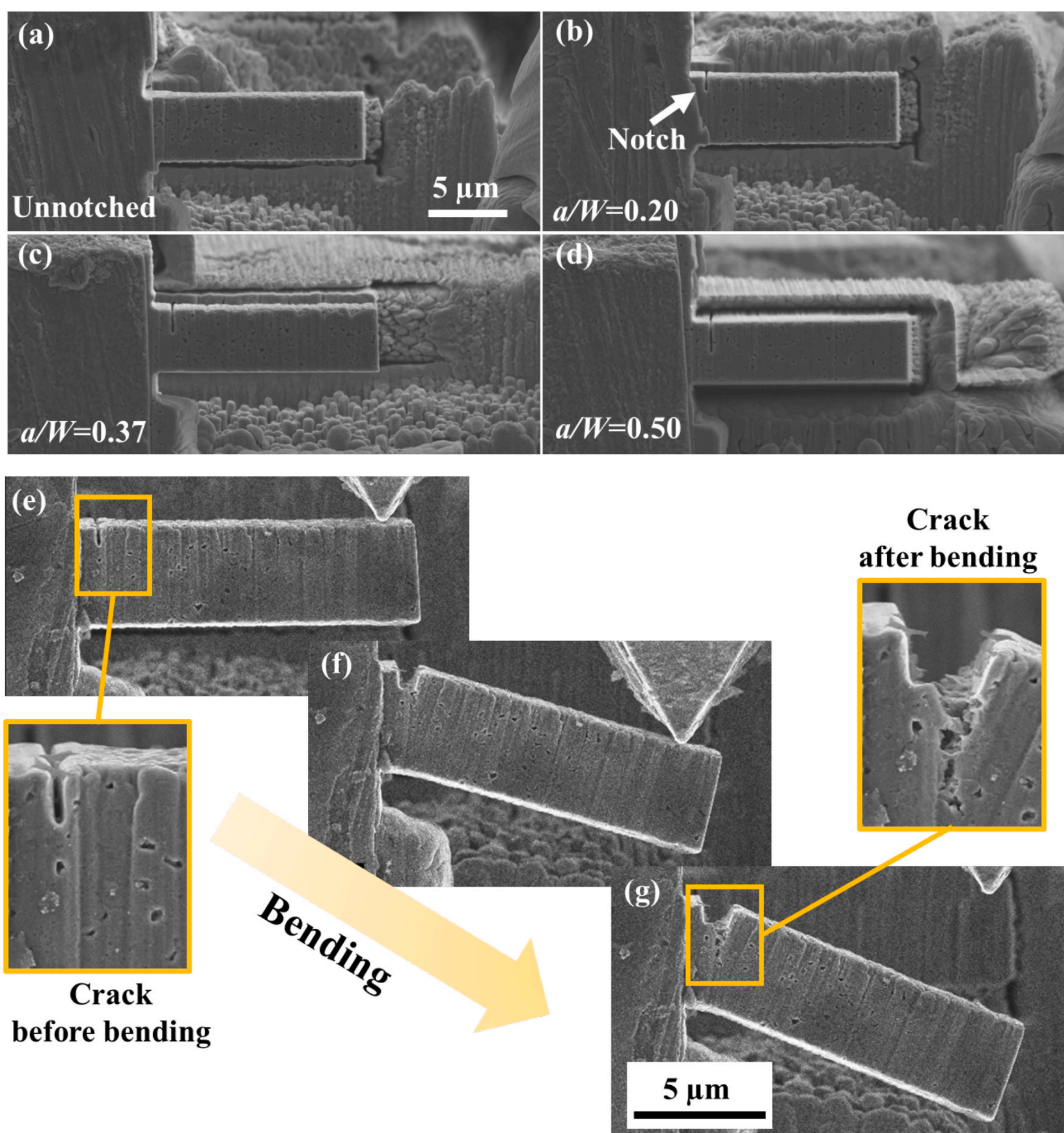

Fig. 4. SEM images of sintered Cu NP cantilever with different a/W ratios (a) a/W = 0; (b) a/W = 0.20; (c) a/W = 0.37; (d) a/W = 0.50; An example of crack propagation in the specimen with a/W = 0.20. (e) before bending; (f) notch blunting during bending; (g) after bending.

application of force. As the bending test continued, after significant crack tip blunting (Fig. 4(f)), the fracture occurred at the notch position, and no bending evidence was found in the front part of the MC beams (Fig. 4(g)). Furthermore, no pronounced dislocation slip deformation-induced surface steps were observed during bending, indicating a possible difference from conventional grained Cu [38]. After bending, the notch tip became more blunted than the original geometry, and the crack propagated into the cantilever body with tearing features.

The fracture surface was analyzed in more detail to identify the fracture mechanism, as shown in Fig. 5(a)-(d), whereby dashed yellow frames indicate the pre-crack area. Typical continuous porous networks with highly sintered structures can be found on all fracture surfaces. Furthermore, Fig. 5(e)(f) magnifies the framed area in the fracture surface with a/W ratio of 0.37 and 0.5, respectively. The fracture surfaces present similar fracture morphology reported in the previous tensile and shearing studies, indicating ductile fracture in the MC bending tests [29,39].

Different fracture features are presented at the fracture surface. At first, multiple local ductile necking tips can be found on elongated Cu grains at the fracture surface, as pointed in Fig. 5(f). This implies that individual Cu struts deformed completely plastically until a detachment of two necked sharp tips occurred, which is consistent with previous molecular dynamics simulation results [40]. Furthermore, in Fig. 5(e)–a tearing ridge of dimples with relatively flat edges can also be noticed at the fracture surface, which is caused by the formation of nanograins within the dimple ridge region.

Besides, not all Cu grains showed plastic fracture features. There are also regions where grains detach without apparent plastic necking phenomenon, as pointed out in Fig. 5(f). This can be attributed to the grain boundary sliding in a multi-particle sintered region during deformation [41,42]. In addition, it is also found that some regions seem not to show any evidence of plasticity, suggesting that these were regions around the previous pores.

The inhomogeneous sintered structure is likely to be the reason behind the hybrid evidence of local plastic deformation. Therefore, the dominant fracture mechanism in this material is best described as continuous pore coalescence upon pure plastic deformation of individual Cu struts, independent of the a/W ratios.

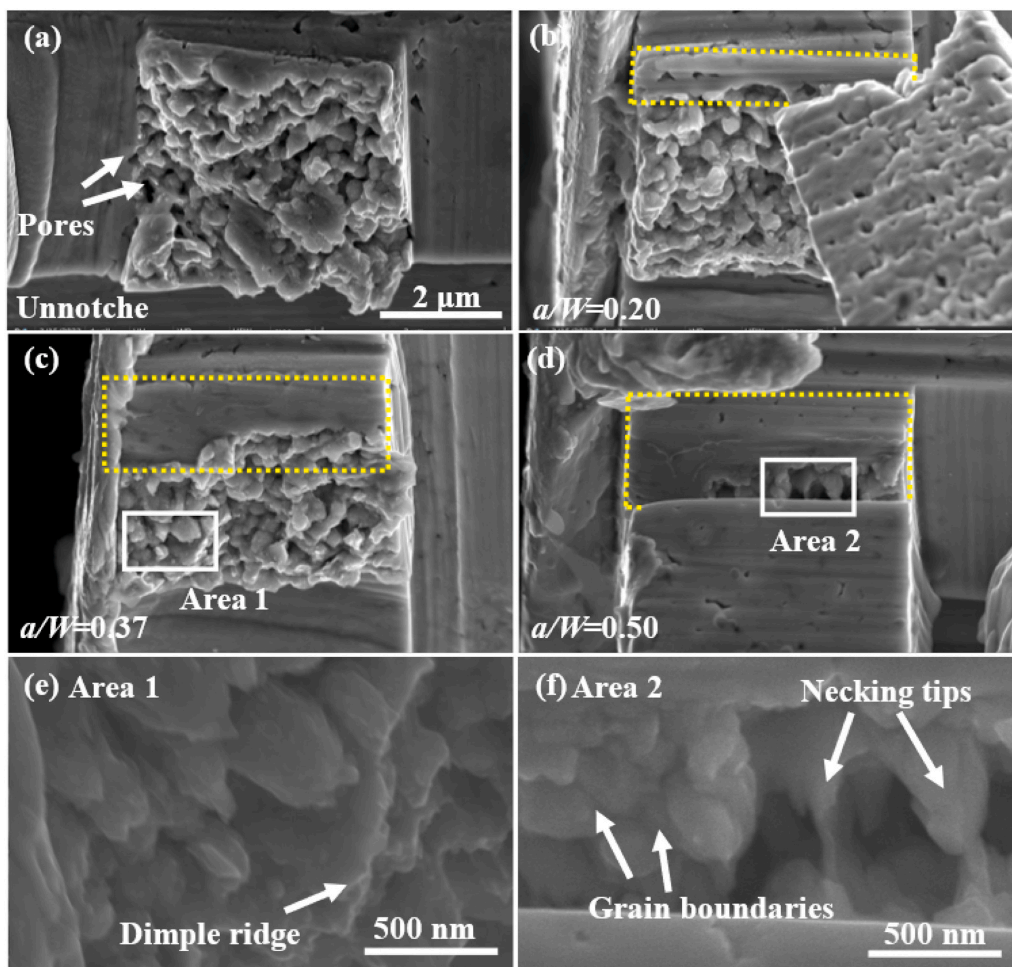

Fig. 5. SEM images of the initial FIB notch area (yellow box) and fracture surface of (a) Unnotched (b) a/W = 0.20 (c) a/W = 0.37 (d) a/W = 0.50 as well as high magnification images of (e) Area 1 and (f) Area 2 framed in (c) and (d), respectively. (For interpretation of the references to colour in this figure legend, the reader is referred to the Web version of this article.)

3.2. Mechanical quantification of sintered Cu micro-cantilevers

Fig. 6(a) presents the load-displacement curves for the unnotched MCs, aW0-01, aW0-02, and aW0-03. An evident yield stage, followed by a decreasing load regime, was observed before failure, indicating a prominent elastic-plastic behavior. This is consistent with the microstructure observation on the fracture surface. Therefore, standard linear elastic fracture mechanics (LEFM) does not apply for the evaluation of fracture toughness $K_{IC,}$ and the more intricate J-integral approach, as described in the experimental section, must be utilized.

The maximum bending stress [35] and strain [43] on the outermost bending fiber of MC is given by linear-elastic bending theory

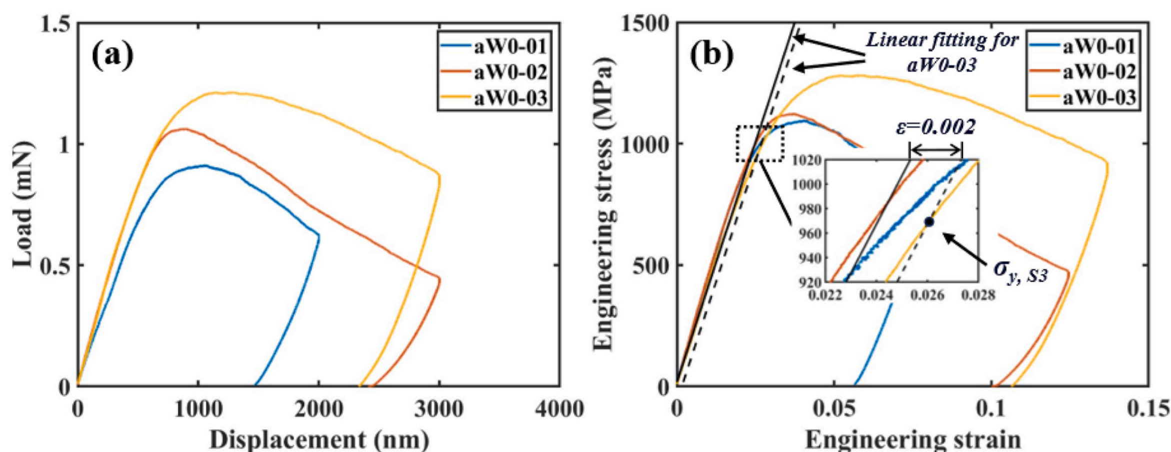

Fig. 6. (a) Load-displacement curves and (b) stress-strain curves of unnotched specimens.

$$\sigma = 6\frac{FL}{BW^2} \quad (8)$$

$$\varepsilon = \frac{3Wu}{2BW^2} \quad (9)$$

with F as the load force, L, B, and W as geometry dimensions defined in Fig. 2, and u as the displacement.

The maximum engineering stress-strain curves of the three unnotched MCs are plotted in Fig. 6(b). A highly reproducible linear elastic initial loading was observed in all specimens. The elastic modulus was calculated from the linear region as 41.42 ± 1.62 GPa. The yield strength was evaluated by plotting the linear fit line with an offset of $\varepsilon =$ 0.002. In doing so, a yield strength of 970 ± 22 MPa was extracted for the sintered structure.

Representative load-displacement results for four different notched MCs are shown in Fig. 7(a), respectively. The initial slope of each curve also depicts a linear elastic regime, followed by evident plastic yielding and a constant flow plateau or slight decrease due to crack extension. The initial slope difference is a result of the difference in initial notch lengths and, therefore, a deviation in the bending ligament. Furthermore, the crack resistance J-Δa curves for different a/W ratios, as calculated using Eqs. (3)–(7), are shown in Fig. 7(b). Three J-Δa curves were presented for each a/W ratio. Fig. 7(c), taking aW20-02 specimen as an example, illustrates the translation from the J-Δa curve to the K_Q.

For the conditional critical J-value evaluation, according to ASTM 1820 [32], a blunting line should be drawn with an offset of 200 μm, which is impossible in this study with micromachined MCs. A analogous 2% W construction was proposed by Pippan et al. [44] and utilized in various publications [45–47]. While it is not a perfect equivalent of the ASTM E1820, it captures the fact that geometric crack tip blunting due to plastic deformation is present. This criterion or similar ones in conjunction with quasi-continuous J-Δa curve measurements have shown agreement in comparison with macroscopic data, where such data exists [30,48]. Therefore, Pippan's 2% W offset criterion was chosen in this study. Segments between 50 and 200 J/m^2 were used to fit the slope of the blunting line because of excellent linearity. J_Q was therefore determined as the intersection of the J-Δa curve and the offset blunting line. The conditional toughness K-value was subsequently calculated using the standard plane stress condition estimate as Eq. (10)

$$K_J = \sqrt{JE} \quad (10)$$

where E is the elastic modulus of the sintered Cu and ν is the Poisson's ratio. This study adopted E = 41.42 GPa as calculated from the unnotched specimens. This was assumed as a lower border estimate for fracture toughness due to the fact that the individual pores as well as the high amount of plastic deformation would lead to an increased content of plane stress condition.

The conditional fracture toughness shows a very shallow increasing trend for longer notch lengths, with values ranging from 3.6 ± 0.1 MPa m$^{1/2}$ for a/W = 0.2 to 3.2 ± 0.3 MPa m$^{1/2}$ for a/W = 0.37 and 4.3 ± 0.1 MPa m$^{1/2}$ for a/W = 0.50, respectively. In macroscopic specimens, it is generally observed that deeply cracked specimens result in lower J-Δa curves because the plastic zone is becoming more constrained [49]. However, an increase in J-Δa behavior has also been observed in macroscopic specimens, where it has been attributed mostly to the loss of plane strain condition [50]. Furthermore, toughness increase with

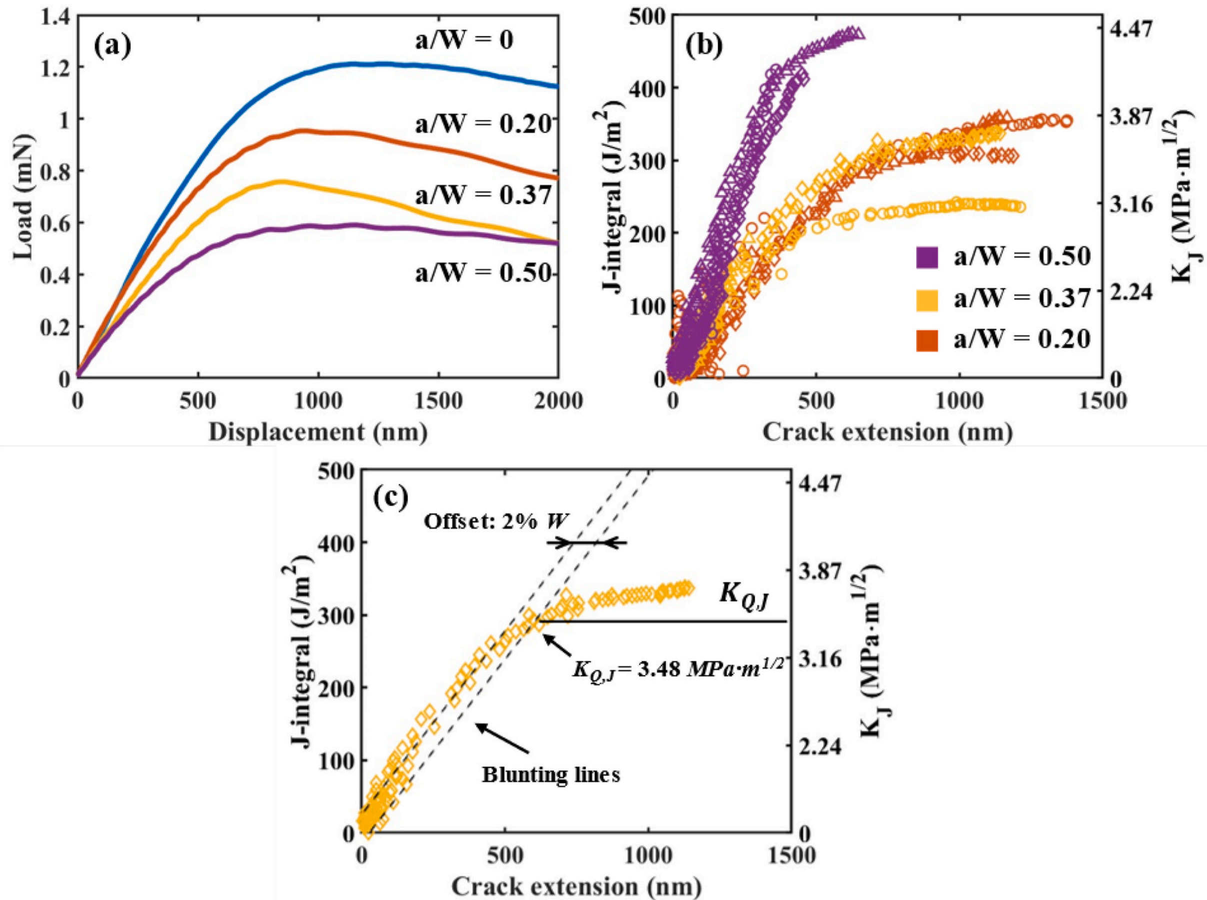

Fig. 7. (a) Representative load-displacement curves; (b) J-Δa curves for the different notched microcantilevers; (c) J-integral evaluation, showing 2% W offset construction. The indices 'Q' refers to the fracture toughness calculated by a blunting line.

increasing notch depth was also reported for similarly scaled W specimen [45], with the stress state and the plastic zone constraint as explanation. However, the good agreement between $a/W = 0.2$ and $a/W = 0.37$ suggests that the change in stress state for lower a/W ratios is not as pronounced as for higher a/W ratios.

4. Discussion

4.1. Plastic zone size considerations

With the known K-value, the plastic zone at the crack tip for plane stress can be determined according to Irwin's model [51,52].

$$R_p = \frac{1}{2\pi}\left(\frac{K_I}{R_e}\right)^2 \tag{11}$$

where R_P is the diameter of the plastic zone, which is assumed as circular, K_I is the stress intensity factor in mode I facture, R_e is the yield strength of 970 ± 22 MPa as calculated above.

To determine the influence of the a/W on the fracture toughness, the relationship between the plastic zone and the remaining length of the ligament must be clarified. Irwin's standard plastic zone size estimation is only a rough approximation. Depending on the local microstructure in front of the crack tip, specifically the arrangement of pores, plastic yielding might be constrained to single struts and not take over the full volume in the crack tip vicinity. While this is not a completely precise description in such heterogeneous systems, it is a useful estimation to assess which fracture mechanics framework (linear-elastic fracture mechanics, elastic plastic fracture mechanics, general yielding) would be appropriate to utilize.

According to Eq. (11), the size of the plastic zone when the K-value reached $K_{Q,J}$ was calculated as 2.14 ± 0.12 μm, 1.74 ± 0.29 μm and 3.1 ± 0.14 μm for $a/W = 0.2$, 0.37 and 0.5, respectively. Compared to the crack extension calculated in Fig. 7(b), it indicates that in the case of $a/W = 0.5$, the entire ligament experienced plastic deformation. This showcases that amount of plastic deformation cannot be ignored and application of purely linear-elastic fracture mechanics, will not be able to yield valid results. For linear-elastic fracture mechanics to hold the plastic zone size should not be larger than roughly 1/25 of the smallest relevant length a, b, B (in analogy to ASTM E399, where the validity criterion would be a, W-a, B > $2.5\cdot(K_I/R_e)^2$) [53]. Hence, the validity criterion to apply liner-elastic fracture mechanics in this case is approximately 60 nm. Even if the microstructural constraint would reduce the plastic zone size by some margin, a reduction from ~2 μm to below 60 nm is not likely. Thus, the plastic zone size estimation should be considered as a classification criterion that indeed elastic-plastic fracture mechanical considerations describe the actual fracture characteristics closer than simplified linear elastic fracture mechanics.

The abovementioned results conclude that the fracture initiation and crack growth in these specimens are governed mainly by the local microstructural characteristics (porosity, grain size, grain cohesion). The fracture characteristics are irrelevant to the notch depth. Besides, as the plastic zone is within the whole ligament length, there is a minor difference between the specimens with $a/W = 0.20$ and 0.37, giving a conditional fracture toughness $K_{Q,J}$ ranging from 3.2 to 3.6 MPa $m^{1/2}$.

4.2. Comparison of Cu with different microstructure

Microscopic fracture toughness has rarely been reported for pure Cu. For example, in high-pressure torsion deformed ultra-fine-grained Cu, a value of 33.4 MPa $m^{1/2}$ was reported, and the initiation toughness decreased according to the refined grain size [54]. However, this high value is hardly applicable in the power electronics die-attachment application, where the bondline thickness is mostly a few tens of micrometers. Regarding the related specimen size effect, Hirakata et al. reported a fracture toughness of 7.81 ± 1.22 MPa $m^{1/2}$ for freestanding 800 nm thickness polycrystalline Cu film [55]. However, unlike the film with a micrometer spanning two-dimensional scale, in the sintered MC, the size effect-induced high-yield stress restrains the plastic deformation in a localized plastic zone, resulting in rupture of individual Cu struts and therefore a lower fracture toughness.

Besides the effect of specimen size on the fracture toughness, porosity also significantly affects the fracture toughness. Well-known classical cell models, e.g., Ashby's [56] and Yang's [57], have been widely used to correlate porosity and fracture toughness. It has been demonstrated that the mode I fracture toughness better satisfied Ashby's model in the case of sintered Ag [19,21,58].

$$K_{IC} = \alpha_1 \sigma_f \sqrt{\pi W}(1-P)^{3/2} \tag{12}$$

where α_1, σ_f, and P are the scaling factor, fracture strength, and porosity, respectively. The fracture toughness remarkably decreases with increased porosity. To date, no mode I fracture toughness is reported in the sintered nanoporous Cu. However, due to the same technological principle, sintered porous Cu has a similar microstructure to that of the sintered porous Ag, including a single metal phase, no preferred orientation, nano-to-submicron grain sizes, randomly distributed pores, and tuneable porosity. Hence, the correlation between the fracture toughness and porosity is highly likely to be described by Eq. (12) because the fracture toughness is one of the reflections from the microstructure. This is further supported by the fact that solid Cu films with similar grain size of 280 nm but smaller specimen thickness of 493 nm already show an increased fracture toughness of 6.6 MPa $m^{1/2}$ [55]. The herein determined fracture toughness values of ~3 MPa $m^{1/2}$ are closer to measured values of sub-100 nm solid Cu films at 2.3 MPa $m^{1/2}$ [55] or severely geometrically restricted transmission electron microscopy specimens (116 nm thickness) of large grained Cu at 3.2 MPa $m^{1/2}$ [46]. All of this suggests that the fracture in the given nanporous Cu is mainly governed by rupture of individual struts with a similar size than such geometrically limited systems.

4.3. Comparison of different die-attach materials

Furthermore, the fracture toughness obtained from micro-cantilever experiments of die-attach materials has been reported over the last decade. The comparison between different die-attach materials is scattered in Fig. 8, including solder materials, such as Cu_3Sn [26], Cu_6Sn_5 [59], AuSn [60] and SAC305 [25], and porous sintered Ag materials [27]. It can be seen that the sintered Cu joint is tougher than the soft Cu–Sn and Au–Sn solders, except SAC305. Additionally, it can be seen that the micron scaled specimen show a size effect with regards to fracture behaviour due to the constraint of plastic zone size and the transition from a plane-strain dominated to a plane-stress dominated behavior [45,61]. This effect is not only the different materials but also more importantly, the different specimen sizes lead to a change in experimentally obtained fracture toughness. Although the value obtained in this work is slightly smaller than the trend of sintered Ag materials, the data in Ref. [20] was calculated from the maximum load during each experiment, neglecting any blunting line offset or R-curve type behaviour and is thus not trimmed towards a safe lower bound for fracture toughness estimations.

Moreover, Cu has a smaller coefficient of thermal expansion (CTE) of 16.6×10^{-6} °C^{-1} than the value of Ag as 18.4×10^{-6} °C^{-1} in comparison to SiC at 4.7×10^{-6} °C^{-1} as common die material. Therefore, lower thermal stresses will be accumulated at the interface during device operation [62]. Thus, the slightly reduced fracture toughness is believed capable of withstanding standard operation environments. Accounting for the cost-effectiveness and anti-electrochemical migration performance, sintered Cu materials can be a potential alternative to the sintered Ag as die-attach materials. Moreover, this work is helpful to the system-level modelling by digging into the fracture behavior of the sintered Cu joint.

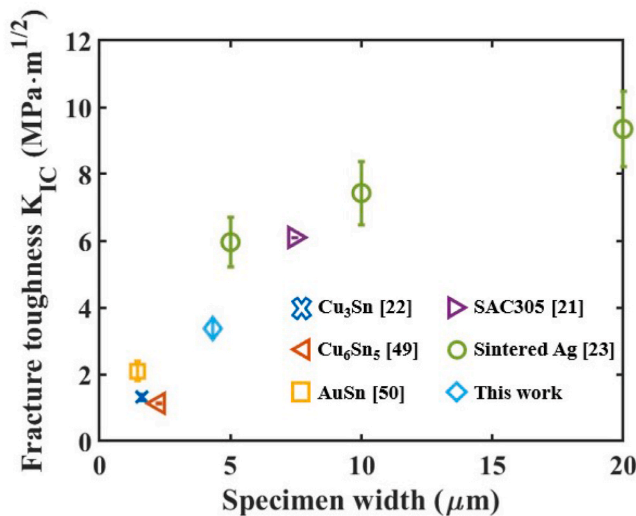

Fig. 8. Fracture toughness of reported die-attach materials with different micro-cantilever specimen widths.

5. Conclusion

The microscopic fracture behaviors of sintered Cu joint are fundamental focuses to evaluate the remaining useful lifetime (RUL) of a die-attach layer in the power electronics packaging. In this study, we developed an experimental method for evaluating crack propagation behavior at a micro-scale in a sintered nanoporous Cu joint by micro-fabricating micro-cantilevers with different notch depths. The following conclusions were obtained:

1) A 3D sintered Cu model was reconstructed by a FIB milling method. The sintered Cu nanoparticle structure yielded a low porosity of 8.25 ± 0.69 %. Necking tips and dimple ridges were observed on the fracture surface, confirming elastic-plastic fracture in the bending test. MCs' elastic modulus and yield strength were extracted as 41 ± 2 GPa and 970 ± 21 MPa, respectively.
2) In-situ microscale measurements of J-Δa curves were carried out on different notched ($a/W \sim 0.20$, 0.37, and 0.50) specimens. Specimens with an a/W ratio of 0.20 and 0.37 presented a close bending behavior. A tougher fracture was noticed with a higher a/W value of 0.5. Instead of the LEFM theory, the microscopic conditional fracture toughness K_Q was translated from elastic-plastic J-integral evaluation, ranging from 3.2 ± 0.3 MPa m$^{1/2}$ to 4.3 ± 0.1 MPa m$^{1/2}$.
3) The microscopic fracture toughness presents a limited relationship with notch depth. A relative initial notch depth a/W between 0.20 and 0.37 shows a near-constant fracture toughness. This provides insights into the testing conditions for future testing on the thermally aged specimens and the study on the size effect.

CRediT authorship contribution statement

Dong Hu: Writing – review & editing, Writing – original draft, Funding acquisition, Formal analysis, Conceptualization. **Leiming Du:** Writing – review & editing, Resources, Methodology, Conceptualization. **Markus Alfreider:** Writing – review & editing, Resources, Methodology, Conceptualization. **Jiajie Fan:** Writing – review & editing, Supervision. **Daniel Kiener:** Writing – review & editing, Supervision, Resources, Methodology. **Guoqi Zhang:** Writing – review & editing, Supervision, Project administration, Funding acquisition.

Declaration of competing interest

The authors declare that they have no known competing financial interests or personal relationships that could have appeared to influence the work reported in this paper.

Data availability

Data will be made available on request.

Acknowledgments

The authors would like to thank Xiao Hu of Delft University of Technology for the support of 3D reconstruction. This work was supported by the ECSEL Joint Undertaking (JU) under grant agreement No 826417. The JU receives support from the European Union's Horizon 2020 research and innovation programme and Germany, Austria, Spain, Finland, Hungary, Slovakia, Netherlands, Switzerland. This project has received funding from the European Research Council (ERC) under the European Union's Horizon 2020 research and innovation programme (Grant No. 771146 TOUGHIT). This project was supported by National Natural Science Foundation of China (Grant No. 52275559).

References

[1] G.Q. Zhang, M. Graef, F. Van Roosmalen, Strategic research agenda of "more than Moore,", in: 7th Int. Conf. Therm. Mech. Multiphysics Simul. Exp. Micro-electronics Micro-systems, EuroSimE 2006, vol. 2006, 2006, pp. 1–6, https://doi.org/10.1109/ESIME.2006.1644043.
[2] U.S. Department of Energy, Electrical and Electronics Technical Team Roadmap, U. S. DRIVE Partnersh., 2017.
[3] H. Lee, V. Smet, R. Tummala, A review of SiC power module packaging technologies: challenges, advances, and emerging issues, IEEE J. Emerg. Sel. Top. Power Electron. 8 (2020) 239–255, https://doi.org/10.1109/JESTPE.2019.2951801.
[4] A. Matallana, E. Ibarra, I. López, J. Andreu, J.I. Garate, X. Jordà, J. Rebollo, Power module electronics in HEV/EV applications: new trends in wide-bandgap semiconductor technologies and design aspects, Renew. Sustain. Energy Rev. 113 (2019) 109264, https://doi.org/10.1016/j.rser.2019.109264.
[5] H. Zhang, J. Minter, N. Lee, A brief review on high-temperature , Pb-free die-attach materials, J. Electron. Mater. 48 (2019) 201–210, https://doi.org/10.1007/s11664-018-6707-6.
[6] P.P. Paret, D.J. DeVoto, S.V.J. Narumanchi, Thermomechanical modeling of high-temperature bonded interface materials, in: Die-Attach Mater. High Temp. Appl. Microelectron. Packag. Mater. Process. Equipment, Reliab., 2019, https://doi.org/10.1007/978-3-319-99256-3_4.
[7] K.S. Siow, Die-Attach Materials for High Temperature Applications in Microelectronics Packaging, 2019.
[8] V.R. Manikam, K.Y. Cheong, Die attach materials for high temperature applications: a review, IEEE Trans. Compon. Packag. Manuf. Technol. 1 (2011) 457–478, https://doi.org/10.1109/TCPMT.2010.2100432.
[9] C. Ding, H. Liu, K.D.T. Ngo, R. Burgos, G.Q. Lu, A double-side cooled SiC MOSFET power module with sintered-silver interposers: I-design, simulation, fabrication, and performance characterization, IEEE Trans. Power Electron. 36 (2021) 11672–11680, https://doi.org/10.1109/TPEL.2021.3070326.
[10] A. Tablati, N. Alayli, T. Youssef, O. Belnoue, L. Theolier, E. Woirgard, New power module concept in PCB-embedded technology with silver sintering die attach, Microelectron. Reliab. 114 (2020), https://doi.org/10.1016/j.microrel.2020.113891.
[11] M. Schaal, M. Klingler, B. Wunderle, Silver Sintering in Power Electronics: the State of the Art in Material Characterization and Reliability Testing, in: 2018 7th Electron, Syst. Technol. Conf. ESTC 2018 - Proc., 2018, https://doi.org/10.1109/ESTC.2018.8546498.
[12] R. Riva, C. Buttay, B. Allard, P. Bevilacqua, Migration issues in sintered-silver die attaches operating at high temperature, in: Microelectron, Reliab., 2013, https://doi.org/10.1016/j.microrel.2013.07.103.
[13] K. Yasui, S. Hayakawa, M. Nakamura, D. Kawase, T. Ishigaki, K. Sasaki, T. Tabata, T. Morita, M. Sagawa, H. Matsushima, T. Kobayashi, Improvement of power cycling reliability of 3.3kV full-SiC power modules with sintered copper technology for Tj, max=175°C, in: Proc. Int. Symp. Power Semicond. Devices ICs, 2018, https://doi.org/10.1109/ISPSD.2018.8393701.
[14] T.F. Chen, K.S. Siow, Comparing the mechanical and thermal-electrical properties of sintered copper (Cu) and sintered silver (Ag) joints, J. Alloys Compd. 866 (2021) 158783, https://doi.org/10.1016/j.jallcom.2021.158783.
[15] Y. Tan, X. Li, X. Chen, Fatigue and dwell-fatigue behavior of nano-silver sintered lap-shear joint at elevated temperature, Microelectron. Reliab. 54 (2014) 648–653, https://doi.org/10.1016/j.microrel.2013.12.007.
[16] H. Zhang, W. Wang, H. Bai, G. Zou, L. Liu, P. Peng, W. Guo, Microstructural and mechanical evolution of silver sintering die attach for SiC power devices during high temperature applications, J. Alloys Compd. 774 (2019) 487–494, https://doi.org/10.1016/j.jallcom.2018.10.067.

[17] F. Le Henaff, S. Azzopardi, J.Y. Deletage, E. Woirgard, S. Bontemps, J. Joguet, A preliminary study on the thermal and mechanical performances of sintered nano-scale silver die-attach technology depending on the substrate metallization, Microelectron. Reliab. 52 (2012) 2321–2325, https://doi.org/10.1016/j.microrel.2012.06.121.
[18] D.J. Devoto, P.P. Paret, A.A. Wereszczak, Stress intensity of delamination in a sintered-silver interconnection, Int. Conf. Exhib. High Temp. Electron. HiTEC 2014 (2014) 296–303, https://doi.org/10.4071/hitec-wa26.
[19] S. Wang, C. Kirchlechner, L. Keer, G. Dehm, Y. Yao, Interfacial fracture toughness of sintered hybrid silver interconnects, J. Mater. Sci. 55 (2020) 2891–2904, https://doi.org/10.1007/s10853-019-04212-1.
[20] S. Zhao, Y. Dai, F. Qin, Y. Li, L. Liu, Z. Zan, T. An, P. Chen, Y. Gong, Y. Wang, On mode II fracture toughness of sintered silver based on end-notch flexure (ENF) test considering various sintering parameters, Mater. Sci. Eng. A. 823 (2021) 141729, https://doi.org/10.1016/j.msea.2021.141729.
[21] Y. Dai, Z. Zan, S. Zhao, F. Qin, Mode II cohesive zone law of porous sintered silver joints with nickel coated multiwall carbon nanotube additive under ENF test, Theor. Appl. Fract. Mech. 121 (2022) 103498, https://doi.org/10.1016/j.tafmec.2022.103498.
[22] J. Ast, M. Göken, K. Durst, Size-dependent fracture toughness of tungsten, Acta Mater. 138 (2017) 198–211, https://doi.org/10.1016/j.actamat.2017.07.030.
[23] K. Matoy, H. Schönherr, T. Detzel, T. Schöberl, R. Pippan, C. Motz, G. Dehm, A comparative micro-cantilever study of the mechanical behavior of silicon based passivation films, Thin Solid Films 518 (2009) 247–256, https://doi.org/10.1016/j.tsf.2009.07.143.
[24] S. Wurster, C. Motz, R. Pippan, Characterization of the fracture toughness of micro-sized tungsten single crystal notched specimens, Philos. Mag. A 92 (2012) 1803–1825, https://doi.org/10.1080/14786435.2012.658449.
[25] Y. Shi, G. Li, C. Peng, W. Zhu, H. He, Microscale fracture toughness degradation of notched solder microcantilevers under varied accelerated aging process, J. Mater. Res. Technol. 22 (2023) 1449–1461, https://doi.org/10.1016/j.jmrt.2022.12.015.
[26] B. Philippi, K. Matoy, J. Zechner, C. Kirchlechner, G. Dehm, Microcantilever fracture testing of intermetallic Cu3Sn in lead-free solder interconnects, J. Electron. Mater. 46 (2017) 1607–1611, https://doi.org/10.1007/s11664-016-5203-0.
[27] C. Chen, S. Nagao, K. Suganuma, J. Jiu, T. Sugahara, H. Zhang, T. Iwashige, K. Sugiura, K. Tsuruta, Macroscale and microscale fracture toughness of microporous sintered Ag for applications in power electronic devices, Acta Mater. 129 (2017) 41–51, https://doi.org/10.1016/j.actamat.2017.02.065.
[28] L. Du, D. Hu, R. Poelm, W. Van Driel, K. Zhang, Micro-cantilever bending test of sintered Cu nanoparticles for power electronic devices, 2023 24th, Int. Conf. Therm. Mech. Multi-Physics Simul. Exp. Microelectron. Microsystems, EuroSimE 2023 (2023), https://doi.org/10.1109/EuroSimE56861.2023.10100756.
[29] D. Hu, C. Qian, X. Liu, L. Du, Z. Sun, X. Fan, G. Zhang, J. Fan, High temperature viscoplastic deformation behavior of sintered nanocopper paste used in power electronics packaging: insights from constitutive and multi-scale modelling, J. Mater. Res. Technol. 26 (2023) 3183–3200, https://doi.org/10.1016/j.jmrt.2023.08.086.
[30] M. Alfreider, D. Kozic, O. Kolednik, D. Kiener, In-situ elastic-plastic fracture mechanics on the microscale by means of continuous dynamical testing, Mater. Des. 148 (2018) 177–187, https://doi.org/10.1016/j.matdes.2018.03.051.
[31] A. Pineau, A.A. Benzerga, T. Pardoen, Failure of metals I: brittle and ductile fracture, Acta Mater. 107 (2016) 424–483, https://doi.org/10.1016/j.actamat.2015.12.034.
[32] ASTM Standard E1820, Standard Test Method for Measurement of Fracture Toughness, ASTM B. Stand., Copyright, 2013, https://doi.org/10.1520/E1820-13.
[33] M. Alfreider, S. Kolitsch, S. Wurster, D. Kiener, An analytical solution for the correct determination of crack lengths via cantilever stiffness, Mater. Des. 194 (2020) 108914, https://doi.org/10.1016/j.matdes.2020.108914.
[34] M. Alfreider, J. Zechner, D. Kiener, Addressing fracture properties of individual constituents within a Cu-WTi-SiOx-Si multilayer, JOM 72 (2020) 4551–4558, https://doi.org/10.1007/s11837-020-04444-6.
[35] A. Riedl, R. Daniel, M. Stefenelli, T. Schöberl, O. Kolednik, C. Mitterer, J. Keckes, A novel approach for determining fracture toughness of hard coatings on the micrometer scale, Scripta Mater. 67 (2012) 708–711, https://doi.org/10.1016/j.scriptamat.2012.06.034.
[36] O. Kolednik, M. Sistaninia, S. Kolitsch, J-integral testing on micro-scale cantilever beam specimens, Eng. Fract. Mech. 292 (2023) 109636, https://doi.org/10.1016/j.engfracmech.2023.109636.
[37] X. Hu, H.A. Martina, R.H. Poelma, J.L. Huang, H. Rijckevorsel, H. Scholten, E.C. P. Smits, W.D. Van Driel, G.Q. Zhang, Microstructure analysis based on 3D reconstruction model and transient thermal impedance measurement of resin-reinforced sintered Ag layer for high power RF device, in: 2023 24th Int. Conf. Therm. Mech. Multi-Physics Simul. Exp. Microelectron. Microsystems, EuroSimE 2023, 2023, https://doi.org/10.1109/EuroSimE56861.2023.10100799.
[38] C. Motz, T. Schöberl, R. Pippan, Mechanical properties of micro-sized copper bending beams machined by the focused ion beam technique, Acta Mater. 53 (2005) 4269–4279, https://doi.org/10.1016/j.actamat.2005.05.036.
[39] X. Liu, S. Li, J. Fan, J. Jiang, Y. Liu, H. Ye, G. Zhang, Microstructural evolution, fracture behavior and bonding mechanisms study of copper sintering on bare DBC substrate for SiC power electronics packaging, J. Mater. Res. Technol. 19 (2022) 1407–1421, https://doi.org/10.1016/j.jmrt.2022.05.122.
[40] D. Hu, Z. Cui, J. Fan, X. Fan, G. Zhang, Thermal kinetic and mechanical behaviors of pressure-assisted Cu nanoparticles sintering: a molecular dynamics study, Results Phys. 19 (2020) 103486, https://doi.org/10.1016/j.rinp.2020.103486.
[41] T. Herboth, M. Guenther, A. Fix, J. Wilde, Failure mechanisms of sintered silver interconnections for power electronic applications, in: Proc. - Electron. Components Technol. Conf, 2013, https://doi.org/10.1109/ECTC.2013.6575789.
[42] A. Abedini, A. Malti, A. Kardani, A. Montazeri, Probing neck growth mechanisms and tensile properties of sintered multi-nanoparticle Al-Cu systems via MD simulation, Adv. Powder Technol. 34 (2023) 104084, https://doi.org/10.1016/j.apt.2023.104084.
[43] M. Wurmshuber, S. Jakob, S. Doppermann, S. Wurster, R. Bodlos, L. Romaner, V. Maier-Kiener, D. Kiener, Tuning mechanical properties of ultrafine-grained tungsten by manipulating grain boundary chemistry, Acta Mater. 232 (2022) 117939, https://doi.org/10.1016/j.actamat.2022.117939.
[44] R. Pippan, S. Wurster, D. Kiener, Fracture mechanics of micro samples: fundamental considerations, Mater. Des. 159 (2018) 252–267, https://doi.org/10.1016/j.matdes.2018.09.004.
[45] A.K. Saxena, S. Brinckmann, B. Völker, G. Dehm, C. Kirchlechner, Experimental conditions affecting the measured fracture toughness at the microscale: notch geometry and crack extension measurement, Mater. Des. 191 (2020) 108582, https://doi.org/10.1016/j.matdes.2020.108582.
[46] M. Alfreider, G. Balbus, F. Wang, J. Zechner, D.S. Gianola, D. Kiener, Interface mediated deformation and fracture of an elastic–plastic bimaterial system resolved by in situ transmission scanning electron microscopy, Mater. Des. 223 (2022) 111136, https://doi.org/10.1016/j.matdes.2022.111136.
[47] A.K. Saxena, A. Kumar, M. Herbig, S. Brinckmann, G. Dehm, C. Kirchlechner, Micro fracture investigations of white etching layers, Mater. Des. 180 (2019), https://doi.org/10.1016/j.matdes.2019.107892.
[48] J. Ast, B. Merle, K. Durst, M. Göken, Fracture toughness evaluation of NiAl single crystals by microcantilevers - a new continuous J-integral method, J. Mater. Res. 31 (2016), https://doi.org/10.1557/jmr.2016.393.
[49] X.K. Zhu, J.A. Joyce, Review of fracture toughness (G, K, J, CTOD, CTOA) testing and standardization, Eng. Fract. Mech. 85 (2012) 1–46, https://doi.org/10.1016/j.engfracmech.2012.02.001.
[50] X.K. Zhu, J.A. Joyce, J-Resistance curve testing of HY80 steel using SE(B) specimens and normalization method, Eng. Fract. Mech. 74 (2007) 2263–2281, https://doi.org/10.1016/j.engfracmech.2006.10.018.
[51] G.R. Irwin, Plastic zone near a crack and fracture toughness, in: Sagamore Res, Conf. Proc., 1961, pp. 63–78.
[52] J.J. Zhang, Applied Petroleum Geomechanics, 2019, https://doi.org/10.1016/C2017-0-01969-9.
[53] ASTM E399, ASTM, Standard Test Method for Linear-Elastic Plane-Strain Fracture Toughness K Ic of of Metallic Materials 399-12, E399, ASTM B. Stand., 2013, p. 399, 2013.
[54] A. Hohenwarter, R. Pippan, A comprehensive study on the damage tolerance of ultrafine-grained copper, Mater. Sci. Eng. 540 (2012) 89–96, https://doi.org/10.1016/j.msea.2012.01.089.
[55] H. Hirakata, O. Nishijima, N. Fukuhara, T. Kondo, A. Yonezu, K. Minoshima, Size effect on fracture toughness of freestanding copper nano-films, Mater. Sci. Eng. 528 (2011) 8120–8127, https://doi.org/10.1016/j.msea.2011.07.071.
[56] M.F. Ashby, Mechanical properties of cellular solids., Metall. Trans. A, Phys. Metall. Mater. Sci. 14 A (1983) 1755–1769. doi:10.1007/BF02645546.
[57] J.F. Yang, T. Ohji, S. Kanzaki, A. Díaz, S. Hampshire, Microstructure and mechanical properties of silicon nitride ceramics with controlled porosity, J. Am. Ceram. Soc. 85 (2002) 1512–1516, https://doi.org/10.1111/j.1151-2916.2002.tb00305.x.
[58] Y. Dai, L. Zhao, Z. Zan, F. Qin, Mode I fracture of sintered nano-silver doped with nickel-coated multiwall carbon nanotube, Mater. Sci. Semicond. Process. 174 (2024) 108171, https://doi.org/10.1016/j.mssp.2024.108171.
[59] B. Philippi, K. Matoy, J. Zechner, C. Kirchlechner, G. Dehm, Fracture toughness of intermetallic Cu6Sn5 in lead-free solder microelectronics, Scripta Mater. 123 (2016) 38–41, https://doi.org/10.1016/j.scriptamat.2016.05.039.
[60] C. Du, R. Soeler, B. Völker, K. Matoy, J. Zechner, G. Langer, M. Reisinger, J. Todt, C. Kirchlechner, G. Dehm, Au–Sn solders applied in transient liquid phase bonding: microstructure and mechanical behavior, Materialia 8 (2019) 100503, https://doi.org/10.1016/j.mtla.2019.100503.
[61] M. Wurmshuber, M. Alfreider, S. Wurster, M. Burtscher, R. Pippan, D. Kiener, Small-scale fracture mechanical investigations on grain boundary doped ultrafine-grained tungsten, Acta Mater. 250 (2023), https://doi.org/10.1016/j.actamat.2023.118878.
[62] B. Seligmann, M. Alfreider, M. Wurmshuber, D. Kiener, Novel approach for assessing cyclic thermomechanical behavior of multilayered structures, Adv. Eng. Mater. 25 (2023) 1–11, https://doi.org/10.1002/adem.202201209.